Monthly Notices of the ROYAL ASTRONOMICAL SOCIETY

Mon. Not. R. Astron. Soc. **406,** 1875–1884 (2010) doi:10.1111/j.1365-2966.2010.16782.x

Dependence of the star formation efficiency on global parameters of molecular clouds

Yetli Rosas-Guevara,[1★] Enrique Vázquez-Semadeni,[1★] Gilberto C. Gómez[1★] and A.-Katharina Jappsen[2★]

[1]*Centro de Radioastronomía y Astrofísica, Universidad Nacional Autónoma de México, Apdo. Postal 3-72, Morelia, 58089, México*
[2]*School of Physics and Astronomy, Cardiff University, Queens Buildings, The Parade, Cardiff CF24 3AA*

Accepted 2010 April 2. Received 2010 February 9; in original form 2009 August 8

ABSTRACT

We investigate the response of the star formation efficiency (SFE) to the main parameters of simulations of molecular cloud formation and evolution (growth and star formation) by the collision of warm diffuse medium [warm neutral medium (WNM)] cylindrical streams, and compare our results with theoretical predictions for this dependence. The parameters we vary are the Mach number of the inflow velocity of the streams, $\mathcal{M}_{\rm s,inf}$, the rms Mach number, $\mathcal{M}_{\rm s,bgd}$, of the initial background turbulence in the WNM and the total mass contained in the colliding gas streams, $M_{\rm inf}$, which is eventually deposited in the forming clouds. Because the SFE is a function of time, we define two estimators for it, the 'absolute' SFE, measured at $t = 25$ Myr into the simulation's evolution (SFE$_{\rm abs,25}$), and the 'relative' SFE, measured 5 Myr after the onset of star formation in each simulation (SFE$_{\rm rel,5}$). The latter is close to the 'SFE per free-fall time' for gas at $n = 100\,{\rm cm}^{-3}$. Our simulations suggest that the dominant parameter controlling the SFE is $M_{\rm inf}$. The SFE in general decreases as this parameter is decreased, presumably because, with the other parameters being equal, smaller fragments are more weakly gravitationally bound. In terms of the initial virial parameter ($\alpha \equiv 2E_{\rm kin}/|E_{\rm grav}|$) of the clouds, our results are qualitatively consistent with the theoretical prediction by Krumholz & McKee that the SFE decreases with increasing α. However, quantitatively, their prediction lies beyond the 1σ error of our observed trend. This may be due to the fact that the simulated clouds develop significant gravitational contraction motions, which overwhelm the initial turbulent motions, contrary to Krumholz & McKee's assumption of stationary turbulent support. We also observe that the SFE decreases (moderately) with increasing $\mathcal{M}_{\rm s,inf}$, although the SFR increases. The decrease of the SFE with $\mathcal{M}_{\rm s,inf}$ is thus a consequence of the cloud mass accretion rate from the WNM increasing more steeply with this parameter than the SFR. Finally, we find that increasing levels of background turbulence (injected at scales comparable to the streams' transverse radius) similarly reduce the SFE, because the turbulence disrupts the coherence of the colliding streams, fragmenting the cloud and producing small-scale clumps, which again have lower SFEs.

Key words: turbulence – stars: formation – ISM: clouds – local interstellar matter.

1 INTRODUCTION

The control of the star formation efficiency (SFE) by turbulence is a central issue in our present understanding of star formation (SF), and currently a topic of intense study (see e.g. the reviews by Mac Low & Klessen 2004; McKee & Ostriker 2007). In recent years, several groups have studied the SFE of molecular clouds (MCs) using numerical simulations of isothermal turbulence, in which the entire numerical box represents the interior of an MC (see e.g. the reviews by Mac Low & Klessen 2004; Ballesteros-Paredes et al. 2007; Vázquez-Semadeni 2007). One confusing issue is that simulations of driven turbulence seem to indicate that the SFE decreases as the turbulent rms Mach number $\mathcal{M}_{\rm s}$ increases (e.g. Klessen, Heitsch & Mac Low 2000; Vázquez-Semadeni, Ballesteros-Paredes & Klessen 2003; Vázquez-Semadeni, Kim & Ballesteros-Paredes 2005), while simulations of decaying turbulence suggest that the SFE increases

★E-mail: y.rosas@crya.unam.mx (YRG); e.vazquez@crya.unam.mx (EVS); g.gomez@crya.unam.mx (GCG); jappsena@Cardiff.ac.uk (AKJ)

with increasing $\mathcal{M}_s$ (Nakamura & Li 2005). This has prompted the question of how does turbulence actually originate and behave in real MCs. To answer this question, it has become necessary to investigate the entire evolutionary process of MCs.

The formation of MCs by collisions of warm neutral medium (WNM) streams has been intensely studied in recent years. A vast body of numerical simulations has shown that moderate, transonic compressions in the WNM can non-linearly trigger a phase transition to the cold neutral medium (e.g. Hennebelle & Pérault 1999; Koyama & Inutsuka 2000, 2002; Walder & Folini 2000), and that the dense gas produced by this mechanism is overpressured with respect to the mean WNM thermal pressure (Vázquez-Semadeni et al. 2006) and turbulent, due to the combined action of Kelvin–Helmholz, thermal (Field 1965) and non-linear thin-shell (Vishniac 1994) instabilities (Heitsch et al. 2005, 2006). The turbulence produced by this mechanism is continually driven for as long as the compression lasts.

The physical scenario of MC evolution was outlined by Hartmann, Ballesteros-Paredes & Bergin (2001), who estimated the column densities necessary for the cloud to become self-gravitating, molecular and magnetically supercritical, finding them to be comparable. The one-dimensional physical conditions in the dense atomic gas were calculated analytically by Hennebelle & Pérault (1999) and Vázquez-Semadeni et al. (2006). A recent review of the subject has been presented by Hennebelle, Mac Low & Vázquez-Semadeni (2008).

More recently, simulations including self-gravity and 'sink particles', which represent gravitationally collapsed objects (stars or stellar clusters), and using finite-duration compressions in the WNM, although lacking stellar feedback and magnetic fields, have been used to study the evolution of the turbulent motions and of the SFE in a self-consistent manner since the formation of a cloud, and up to the early stages of its star-forming epochs (Vázquez-Semadeni et al. 2007, hereafter Paper I). Concerning the velocity dispersion in the clouds, these authors found that the turbulence is intermediate between driven and decaying, since what decays is the driving rate of the turbulence as the inflows weaken with time. However, they also found that the random motions are gradually replaced by global infall motions, as the cloud begins to contract gravitationally. Concerning the SFE, Paper I measured the masses of dense gas $M_{\rm dense}$ and of the collapsed stellar objects $M_{\rm stars}$ in the simulations, allowing a measurement of the SFE, defined as

$$\mathrm{SFE} = \frac{M_{\rm stars}}{M_{\rm dense} + M_{\rm stars}}. \tag{1}$$

The resulting SFE was however too high, reaching ∼50 per cent roughly 6 Myr after the time at which SF had begun (denoted $t_{\rm SF}$), although this excessive SFE can possibly be attributed to the neglect of stellar feedback in that simulation. Indeed, Paper I estimated, using a prescription by Franco, Shore & Tenorio-Tagle (1994) and a standard initial mass function (IMF) (Kroupa 2001), that by 3 Myr after $t_{\rm SF}$ enough massive stars would have formed as to be able to destroy the cloud by ionization. At that point, the SFE was ∼15 per cent, closer to the typical values $\lesssim$5 per cent reported observationally for full MC complexes (Myers et al. 1986). Moreover, a recent study by Vázquez-Semadeni, Colín & Gómez (2010) using the same physical setup as Paper I, but including a simple prescription for following the effect of feedback from massive star ionization heating, suggested that the evolution is unchanged with respect to that of the simulations from Paper I during the initial stages, until the feedback begins to reduce the SFE. One crucial feature that is preserved upon the inclusion of stellar feedback is the global gravitational contraction of the cloud, which begins *before* the onset of SF. Thus, the main driver of the cloud evolution and its SF activity appears to be the global gravitational contraction of the cloud, while feedback apparently just regulates the *local* (at the level of clumps and cores within the cloud) conversion of gas to stars.

Interestingly, the MC evolutionary path that develops in these simulations is qualitatively very different from traditional ideas that MCs are quasi-equilibrium structures, supported against their self-gravity by a combination of turbulent and magnetic pressures, in which only the dense cores proceed to collapse when they become gravitationally unstable, either because they lose magnetic support through ambipolar diffusion (see e.g. the reviews by Shu, Adams & Lizano 1987; Mouschovias 1991) or because they are pushed into collapse by local turbulent compressions (see e.g. the reviews by Vazquez-Semadeni et al. 2000; Mac Low & Klessen 2004; Ballesteros-Paredes et al. 2007; McKee & Ostriker 2007). The latter scenario, in which a cloud is globally supported by turbulence, but in which clumps are produced by the turbulence, and may collapse if they become smaller than their Jeans length, is at the basis of recent theories for the IMF (Padoan & Nordlund 2002; Padoan et al. 2007) and for the SF rate (Krumholz & McKee 2005, hereafter KM05). Instead, in the numerical simulations of Paper I and Vázquez-Semadeni et al. (2010), the whole cloud, or at least a sizeable fraction of it, is undergoing global contraction and hierarchical gravitational fragmentation, as proposed by various groups (Hartmann & Burkert 2007; Field, Blackman & Keto 2008; Galván-Madrid et al. 2009; Vázquez-Semadeni et al. 2009).

Thus, it is relevant to investigate the response of the SFE, in the colliding flow scenario, to variations of the parameters of the collision, even in the absence of stellar feedback, since the effects of the latter will begin to be felt at late stages in the evolution, but the main driver of the evolution, the global cloud contraction, is due to the properties of the colliding flows. In this paper we undertake a first approach to such task, by varying three parameters of the WNM stream collisions modelled in the simulations. First, we consider the inflow speed $v_{\rm inf}$ and the velocity dispersion of the background turbulence initially present in the medium, both measured by their respective Mach numbers, $\mathcal{M}_{\rm s,inf}$ and $\mathcal{M}_{\rm s,bgd}$, with respect to the unperturbed WNM. Subsequently, we consider the mass in the colliding streams $M_{\rm inf}$, as determined by their radius $R_{\rm inf}$ and length $l_{\rm inf}$. Our results in this regard are then compared with the predictions of KM05 for the SFE. Since the parameter space covered by these three parameters is already quite large, in this work we do not consider variations in the collision angle of the streams, instead having them collide head-on in all cases.

This paper is organized as follows. In Section 2, we describe the numerical model and experiments. In Section 3 we present our results, and in Section 4 we present a summary and our conclusions.

2 NUMERICAL MODEL AND EXPERIMENTS

For the numerical simulations, we use the same numerical setup as that used in Paper I, except that we now use the smoothed particle hydrodynamics (SPH) + N-body code GADGET-2 (Springel 2005) (in Paper I we used the previous version of the code, GADGET), modified to include random turbulence driving and sink particles according to the prescription of Jappsen et al. (2005), and including parametrized heating and cooling, as applied in Paper I, using the fit of Koyama & Inutsuka (2002) to a variety of atomic and molecular cooling processes. This cooling function causes the gas to be thermally unstable, under the isobaric mode, in the density range

Table 1. Run parameters.

Run number	Run name	$L_{\rm box}$ (pc)	$l_{\rm inf}$ (pc)	$v_{\rm inf}$ (km s $^{-1}$)	$\mathcal{M}_{\rm s,inf}$	$\mathcal{M}_{\rm s,bgd}$	$R_{\rm inf}$ (pc)	$M_{\rm box}$ (M$_\odot$)	$M_{\rm inf}$ (M$_\odot$)	$M_{\rm part}$ (M$_\odot$)
1	Mi1-Mb.11-Ma2e4	256	112	9.20	1.25	0.11	32	5.25×10^5	2.26×10^4	0.32
2	Mi2-Mb.11-Ma2e4	256	112	18.41	2.50	0.11	32	5.25×10^5	2.26×10^4	0.32
3	Mi1-Mb.27-Ma2e4	256	112	9.20	1.25	0.27	32	5.25×10^5	2.26×10^4	0.32
4 (Fiducial)	Mi1-Mb.02-Ma2e4	256	112	9.20	1.25	0.021	32	5.25×10^5	2.26×10^4	0.32
5	Mi2-Mb.02-Ma2e4	256	112	18.41	2.50	0.024	32	5.25×10^5	2.26×10^4	0.32
6	Mi3-Mb.02-Ma2e4	256	112	25.77	3.50	0.025	32	5.25×10^5	2.26×10^4	0.32
8	Mi1-Mb.02-Ma5e3	256	112	9.20	1.25	0.020	16	5.25×10^5	5.64×10^3	0.32
10	Mi1-Mb.06-Ma6e2	128	48	9.20	1.25	0.057	8	6.57×10^4	6.04×10^2	0.04
11	Mi0-Mb.10-Ma2e4	256	112	0.	0.	0.10	32	5.25×10^5	2.26×10^4	0.32
12	Mi1-Mb.06-Ma2e3	128	48	9.20	1.25	0.058	16	6.57×10^4	2.42×10^3	0.04

$1 \lesssim n \lesssim 10\,{\rm cm}^{-3}$. We assume that the gas is all atomic,[1] with a mean atomic weight $\mu = 1.27$. The numerical box is periodic, with size $L_{\rm box}$. In all cases, we use $118^3 = 1.64 \times 10^6$ particles and set the mean number of particles within a smoothing volume to 40. According to the criterion of Bate & Burkert (1997), the effective mass resolution of our simulations is twice the number of particles within a smoothing volume or $\sim$80 times the mass per particle. The critical density for sink formation is set at $3.2 \times 10^7\,{\rm cm}^{-3}$, and the outer sink accretion radius is set at 0.04 pc.

An initial turbulent velocity field of one-dimensional velocity dispersion, characterized by its rms Mach number $\mathcal{M}_{\rm s,bgd}$ and applied at scales between 1/4 and 1/8 of the box size, is added to the inflow velocity field, in order to trigger the instabilities that render the cloud turbulent. Note that this added turbulent velocity field is applied by turning on the random driver for the first few time-steps of the simulation's evolution and that what we actually control is the energy injection rate parameter. Thus, simulations intended to have the same turbulence strength do so only approximately, as the flow's response is slightly different in every realization.

The initial conditions consist of a uniform medium at $n = 1\,{\rm cm}^{-3}$ and $T = 5000$ K, in which two cylinders of length $l_{\rm inf}$ along the x direction and radius $R_{\rm inf}$ are set to collide head-on at the $x = L_{\rm box}/2$ plane of the simulation (refer to fig. 1 of Paper I). Note that the cylindrical inflows are entirely contained within the numerical box, since the boundaries are periodic. The length $l_{\rm inf}$ is measured from the central collision plane and is always shorter than the half-length of the box, implying that a small region between the edge of the inflows and the box boundaries is not given any velocity. This region is partially evacuated during the subsequent evolution of the simulations, as the gas within it tends to fill the void left by the inflows. Note that, at the initial density and temperature, the gas is Jeans stable in all of our runs and has no tendency to collapse. However, the collision of the inflows non-linearly triggers the thermal instability (Hennebelle & Pérault 1999; Koyama & Inutsuka 2000; Kritsuk & Norman 2002), producing a cold atomic cloud of density $n \sim 100\,{\rm cm}^{-3}$ at the collision site that soon becomes Jeans unstable and begins to contract gravitationally (Paper I). Note also that the gravitational contraction of the clouds typically begins *before* average physical conditions typical of MCs are reached. That is, the contraction begins during the atomic phase. In fact, it is the gravitational contraction that causes the cloud to reach MC densities.

[1] Our 'MCs' are thus only so in the sense of density and temperature, but not of chemical composition.

Table 1 shows the various runs we performed for the present study, indicating the relevant parameters for each one. In addition to the inflow length, radius and velocity, defined above, Table 1 gives the Mach number $\mathcal{M}_{\rm s,inf}$ corresponding to $v_{\rm inf}$ at the initial temperature of the gas, for which the adiabatic sound speed is 7.54 km s $^{-1}$, the one-dimensional rms Mach number of the initial turbulent motions, $\mathcal{M}_{\rm s,bgd}$, the total mass contained in the simulation box, $M_{\rm box}$, the mass contained in the two inflows, $M_{\rm inf}$, and the mass per SPH particle, $M_{\rm part}$. The runs are labelled mnemonically, with their names giving, in that order, the inflow Mach number $\mathcal{M}_{\rm s,inf}$, the background Mach number $\mathcal{M}_{\rm s,bgd}$ and the inflow mass $M_{\rm inf}$.

Note that run Mi1-Mb.02-Ma2e4 has the same parameters as run L256Δv0.17 from Paper I, and we take these as the 'fiducial' set of parameters. However, the two runs are not identical because they were performed with different codes. GADGET-2 differs in many ways from GADGET and in particular it takes longer time-steps, implying that the initial forcing (used to trigger the instabilities in the dense layer) is applied at different time intervals and with different random seeds. Moreover, run Mi1-Mb.02-Ma2e4 is performed at half the mass resolution as its Paper I counterpart. Thus, the two runs are similar only in a statistical sense. Nevertheless, the general trend of the two runs is indeed the same. Both form a ring at the edge of the circular region where the streams collide, which then begins to contract gravitationally until it starts forming stars after roughly 15 Myr. From this circular ring, radial filaments extend outwards, which at later times form stars too. Finally, at a time between 20 and 25 Myr, the circular ring collapses to the centre. Thus, this reassures us that the general evolution is robust to small variations in the resolution and in the integration scheme. For reference, in Fig. 1 we show a face-on view of run Mi1-Mb.02-Ma2e4 at the time when it is beginning to form stars, showing that the general morphology it develops is similar to that of run L256Δv0.17 from Paper I (compare to fig. 4 of that paper, noting that the linear scales shown are different in the two figures).

We report the SFE as defined by equation (1), with $M_{\rm dense}$ defined as the mass in gas with number density $n \geq 100\,{\rm cm}^{-3}$ and $M_{\rm stars}$ defined as the mass in sink particles. Recall that these form at $n = 3.2 \times 10^7\,{\rm cm}^{-3}$, so $M_{\rm stars}$ is very similar to the mass of gas that has reached these densities, although slightly smaller in general, since additional gravitational binding constraints must be satisfied for a sink to be created by the code (Jappsen et al. 2005). We note that both $M_{\rm dense}$ and $M_{\rm stars}$ are in general functions of time, and thus so is also the SFE.

Because the SFE is a function of time and sink formation in general begins at different times in different runs, in order to report a *number* for the SFE, we estimate it in two different ways. One is to

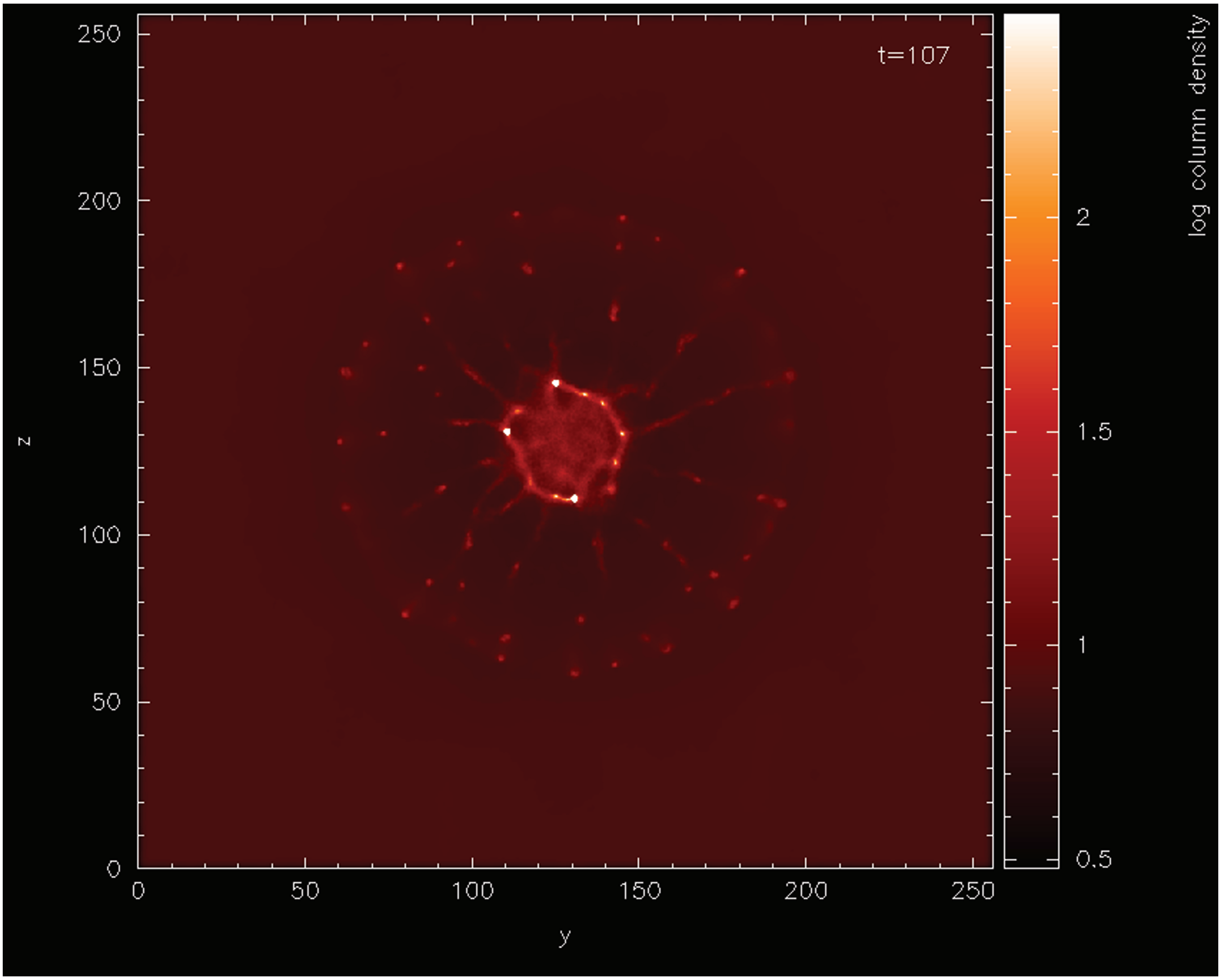

Figure 1. Face-on image in projection of the fiducial run Mi1-Mb.02-Ma2e4 at the time it is beginning to form stars. Note the central ring and the radial filaments, characteristic of this type of runs (Paper I).

measure the 'absolute' SFE 25 Myr after the start of the simulation, which we denote as $\mathrm{SFE}_{\mathrm{abs},25}$. We choose this time because it is sufficiently long for SF to have begun in all runs (albeit barely so in some of them). This estimate thus accounts for any 'dormant' time in the SF activity of the clouds, so that clouds that begin forming stars at later times have lower values of this indicator. The other is to measure the 'relative' SFE, which we define as the SFE 5 Myr after the onset of SF in the simulation and denote as $\mathrm{SFE}_{\mathrm{rel},5}$. This is actually close to the 'star formation rate per free-fall time', $\mathrm{SFR}_{\mathrm{ff}}$ (after SF has begun), as defined by KM05, since the free-fall time for gas at $n \sim 100\,\mathrm{cm}^{-3}$ is ~4.6 Myr.

3 RESULTS

3.1 SFE versus inflow velocity

In this section, we consider the dependence of the SFE on the inflow velocity of the colliding streams, v_{inf}. Fig. 2 shows the evolution of the dense gas mass (left panel) and the sink mass (right panel) for runs Mi1-Mb.02-Ma2e4, Mi2-Mb.02-Ma2e4 and Mi3-Mb.02-Ma2e4. These runs have all parameters equal, except for the speed of the inflows (cf. Table 1), which are varied from $\mathcal{M}_{\mathrm{s,inf}} = 1.25$ in Mi1-Mb.02-Ma2e4 to $\mathcal{M}_{\mathrm{s,inf}} = 3.5$ in Mi3-Mb.02-Ma2e4. Note that the time at which the runs begin to form sinks, t_{SF}, is different in each case. Fig. 3 then shows the SFE, defined as in equation (1). The left panel shows $\mathrm{SFE}_{\mathrm{abs},25}$, i.e. starting from the beginning of the simulation up to a total time of 25 Myr. The right panel shows the SFE starting from the time at which sink formation begins in each run, allowing one to read off $\mathrm{SFE}_{\mathrm{rel},5}$.

From the right-hand panel of Fig. 3 we see that the mean slope (before saturation) of the curve SFE(t), denoted $\langle \dot{\mathrm{SFE}} \rangle$, decreases, although moderately, with increasing $\mathcal{M}_{\mathrm{s,inf}}$. This leads to final efficiencies, $\mathrm{SFE}_{\mathrm{abs},25}$ and $\mathrm{SFE}_{\mathrm{rel},5}$, that *decrease* with increasing $\mathcal{M}_{\mathrm{s,inf}}$, a result summarized by the solid and dashed lines in Fig. 4. On the other hand, the star formation rates (SFRs) of these runs, defined as

$$\mathrm{SFR} \equiv \frac{\mathrm{d}M_{\mathrm{stars}}}{\mathrm{d}t}, \tag{2}$$

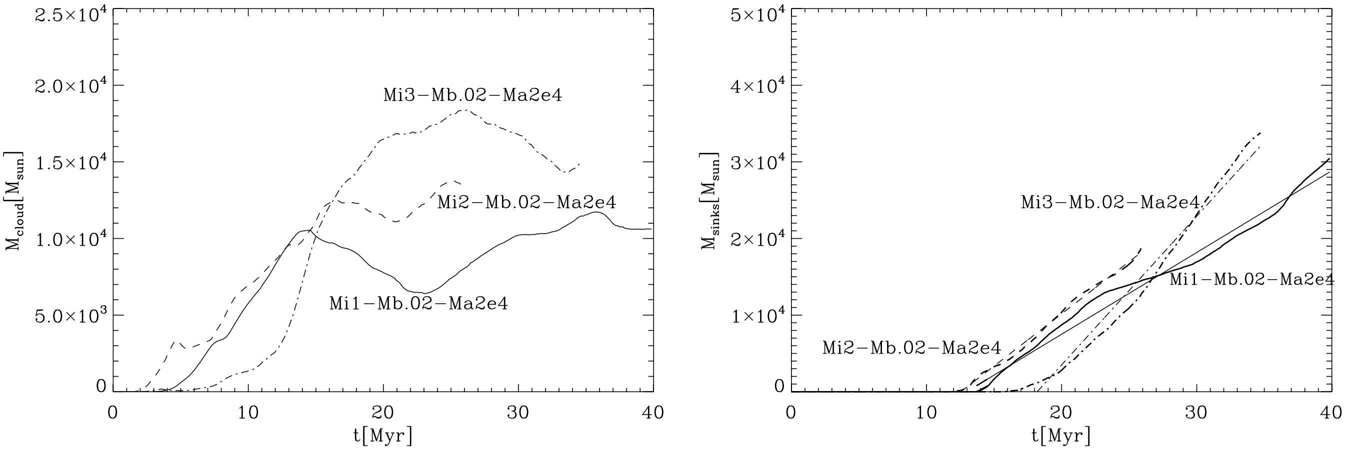

Figure 2. Evolution of the dense gas mass (left-hand panel) and sink mass (right-hand panel) for runs Mi1-Mb.02-Ma2e4, Mi2-Mb.02-Ma2e4 and Mi3-Mb.02-Ma2e4, which differ only by the Mach number of the inflows (indicated by the 'Mi#' entry in the run's name), having $\mathcal{M}_{\rm s,inf} = 1.25$, 2.5 and 3.5, respectively. The thin straight lines in the right-hand panel indicate least-squares fits to the curves.

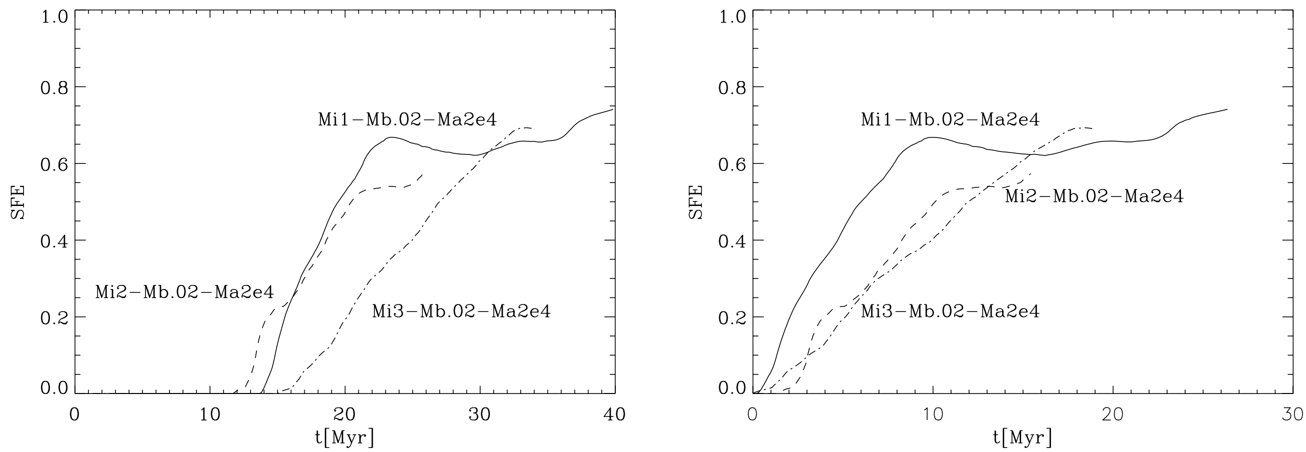

Figure 3. Evolution of the 'absolute' SFE ($\mathrm{SFE}_{\rm abs,25}$, left-hand panel), shown out to 25 Myr after the start of the runs, and the 'relative' SFE (right-hand panel), shown from the onset of sink formation, for runs Mi1-Mb.02-Ma2e4, Mi2-Mb.02-Ma2e4 and Mi3-Mb.02-Ma2e4. $\mathrm{SFE}_{\rm rel,5}$ is the value of this curve at a relative time of 5 Myr.

follow a different trend.[2] The SFR is the slope of the curves in the right-hand panel of Fig. 2, which shows the mass captured in sinks as a function of time for the three runs. We see that the slopes in general increase with increasing $\mathcal{M}_{\rm s,inf}$. Indeed, a least-squares fit to the mean trend of $M_{\rm stars}$ versus time for the three runs (shown by the straight lines in the right-hand panel of Fig. 2) gives the values of $\langle \mathrm{SFR} \rangle$ shown by the dotted line in Fig. 4, with an uncertainty of $\sim$25 per cent. Thus, $\langle \mathrm{SFR} \rangle$ has the opposite trend with $\mathcal{M}_{\rm s,inf}$ to that of the SFE.

This somewhat surprising result can be understood as follows. Both the cloud mass growth rate and the SFR are ultimately driven by the mass conversion rate from the WNM to the cloud caused by the collision of the inflows. This is easy to compute in our simulations, in which the inflows have well-defined (cylindrical) geometry, density and speed. The total rate of mass inflow on to the cloud is thus given by

$$\dot{M}_{\rm c} = 2\rho_{\rm inf} v_{\rm inf} (\pi R_{\rm inf}^2), \quad (3)$$

[2] Note that equation (1) implies that, in general, $\langle \dot{\mathrm{SFE}} \rangle$ is not proportional to the SFR.

where $\rho_{\rm inf} = n_{\rm inf}\,\mu\, m_{\rm H}$ is the inflow mass density, with $n_{\rm inf} = 1\ \mathrm{cm}^{-3}$ being the number density of the inflows, $\mu = 1.27$ the mean atomic weight and $m_{\rm H}$ the hydrogen atomic mass. Moreover, $v_{\rm inf}$ is the inflow speed and $R_{\rm inf}$ is the inflow radius (cf. Table 1). The factor of 2 represents the fact that there are two inflows, one on each side of the (flattened) cloud. We thus obtain

$$\dot{M}_{\rm c} \approx 200 \left(\frac{v_{\rm inf}}{\mathrm{km\,s^{-1}}} \right) \mathrm{M_\odot\ Myr^{-1}}. \quad (4)$$

The values of $\dot{M}$ for the three runs are shown by the dash–dotted line in Fig. 4. Comparing this curve with that for $\langle \mathrm{SFR} \rangle$, it is clear that both increase with $\mathcal{M}_{\rm s,inf}$, but that $M_{\rm c}$ increases faster than $\langle \mathrm{SFR} \rangle$. The decrease in $\langle \dot{\mathrm{SFE}} \rangle$ is thus due to the larger mass growth rate of the cloud induced by the larger inflow velocities, not to a smaller $\langle \mathrm{SFR} \rangle$. Presumably, the larger inflow speed causes a stronger turbulence in the cloud, which in turn causes stronger fragmentation, and thus the net efficiency decreases (cf. Section 3.3), so that enhancement in $\langle \mathrm{SFR} \rangle$ produced by a larger $\mathcal{M}_{\rm s,inf}$ cannot match that induced in $\dot{M}_{\rm c}$.

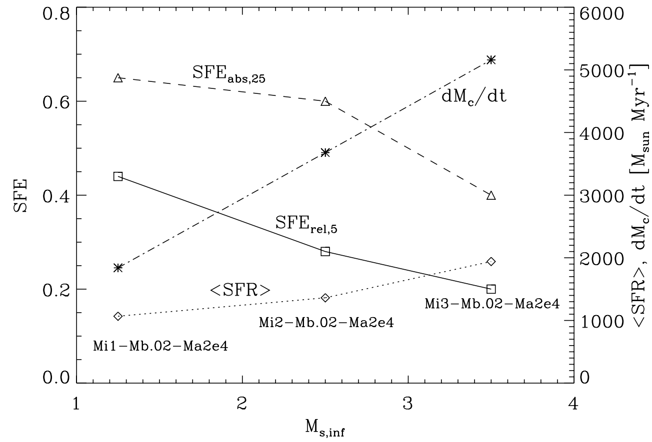

Figure 4. Dependence of efficiencies and rates on the inflow Mach number $\mathcal{M}_{s,\rm inf}$ for runs Mi1-Mb.02-Ma2e4, Mi2-Mb.02-Ma2e4 and Mi3-Mb.02-Ma2e4. Shown are SFE$_{\rm abs,25}$ (dashed line, triangles), SFE$_{\rm rel,5}$ (solid line, squares), the least-squares fit, $\langle$SFR$\rangle$, given by the thin lines in the right-hand panel of Fig. 2, to the SFR (as defined by equation 2) (dotted line, diamonds), and the cloud's mass accretion rate $\dot{M}_{\rm c}$ imposed by the inflow parameters, given by equation (4) (dash–dotted line, asterisks). Both SFEs are seen to decrease with increasing $v_{\rm inf}$, while the SFR and $M_{\rm c}$ increase. The decrease of the SFE with $\mathcal{M}_{s,\rm inf}$ is thus explained because $\dot{M}_{\rm c}$ increases more rapidly with $\mathcal{M}_{s,\rm inf}$ than the SFR (cf. equation 1).

3.2 SFE versus background turbulence strength

We now consider the response of the SFE to the amplitude of the initial turbulent velocity field. Note that this field was not originally intended to produce density condensations on its own, but just to sufficiently disorganize the inflow velocity field as to trigger the instabilities that render the cloud turbulent. However, in the cases of stronger turbulence, we do observe clump formation everywhere in the box as a result of the initial background turbulence, and not just at the collision site of the inflows.

Fig. 5 shows the evolution of the SFE for runs Mi1-Mb.11-Ma2e4, Mi1-Mb.27-Ma2e4, Mi1-Mb.02-Ma2e4 and Mi0-Mb.10-Ma2e4. The first three runs differ only in the strength of the initial turbulence, measured by $\mathcal{M}_{s,\rm bgd}$ (cf. Table 1). The last run has nearly the same value of $\mathcal{M}_{s,\rm bgd}$ as Mi1-Mb.11-Ma2e4, but with no inflow velocity, in order to assess the amount of SF induced solely by the turbulent field, in the absence of colliding streams.

From these figures, we see that $t_{\rm SF}$ becomes longer and $\langle\dot{\rm SFE}\rangle$ becomes smaller as larger values of $\mathcal{M}_{s,\rm bgd}$ are considered. This appears to be due to the stronger fragmentation induced by the turbulent velocity field, which in the extreme case of Mi1-Mb.27-Ma2e4 almost obliterates the inflows and produces scattered clumps throughout the simulation box, with very little remaining of the large, coherent cloud formed by the inflows (as illustrated in Fig. 6, left-hand panel). As shown in Section 3.3, less massive clouds (at the same velocity dispersion and mean density) have smaller efficiencies.

It is also worth noting that run Mi0-Mb.10-Ma2e4, which has no inflows, has a much larger $t_{\rm SF}$ and a lower $\langle\dot{\rm SFE}\rangle$ than run Mi1-Mb.11-Ma2e4, which differs from the former only in the presence of the inflows. As shown in Fig. 6, run Mi0-Mb.10-Ma2e4 also produces scattered clumps throughout the numerical box, although not as profusely as Mi1-Mb.27-Ma2e4. So, we conclude that sink formation is still dominated by the colliding streams in Mi1-Mb.11-Ma2e4, although a fraction of the sinks is contributed by the global turbulence.

Fig. 7 summarizes the results of this section. A clear trend of a decreasing SFE (seen in both SFE$_{\rm abs,25}$ and SFE$_{\rm rel,5}$) with increasing $\mathcal{M}_{s,\rm bgd}$ is seen, which we interpret as a result of the reduction of the fragment mass with increasing turbulence strength (at constant total mass; Ballesteros-Paredes et al. 2006) and of the fact that smaller mass fragments tend to have smaller SFEs (Section 3.3).

3.3 SFE versus inflow mass

The last dependence of the SFE we analyse is on the mass content of the colliding inflows. We consider inflows of various radii. However, since a very narrow inflow is necessarily more poorly resolved, we consider smaller simulation boxes in two of the cases, in order to better resolve the resulting clouds. Specifically, as shown in Table 1, $R_{\rm inf}$ in run Mi1-Mb.02-Ma5e3 is half that in Mi1-Mb.02-Ma2e4. Run Mi1-Mb.06-Ma2e3 has $R_{\rm inf}$ equal to that of Mi1-Mb.02-Ma5e3, but half the length, since the numerical box size of the former is half that of the latter. Finally, Mi1-Mb.06-Ma6e2 has $R_{\rm inf}$ equal to half that of Mi1-Mb.06-Ma2e3. So, the total mass contained in the inflows of runs Mi1-Mb.02-Ma2e4, Mi1-Mb.02-Ma5e3,

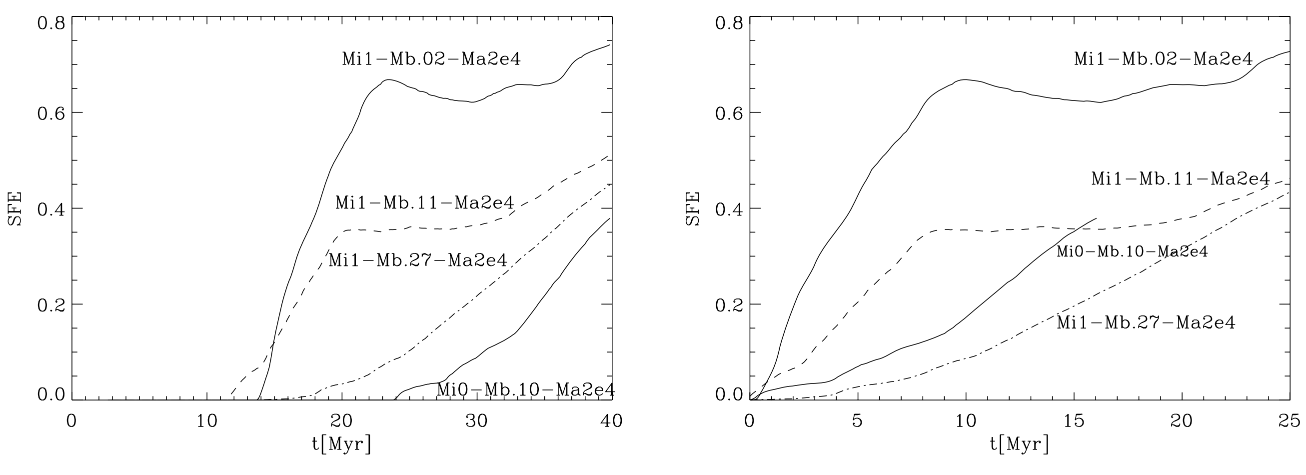

Figure 5. Evolution of the 'absolute' SFE (SFE$_{\rm abs,25}$, left-hand panel) and the 'relative' SFE (right-hand panel) for four runs, characterized by various values of the initial background turbulent Mach number $\mathcal{M}_{s,\rm bgd}$, indicated by the entry 'Mb.##' in the runs' names. Three of the runs have the same inflow Mach number, $M_{\rm inf} = 1.25$, while the fourth run has no inflows ($M_{\rm inf} = 0$), in order to assess the SFE due exclusively to the initial background turbulence.

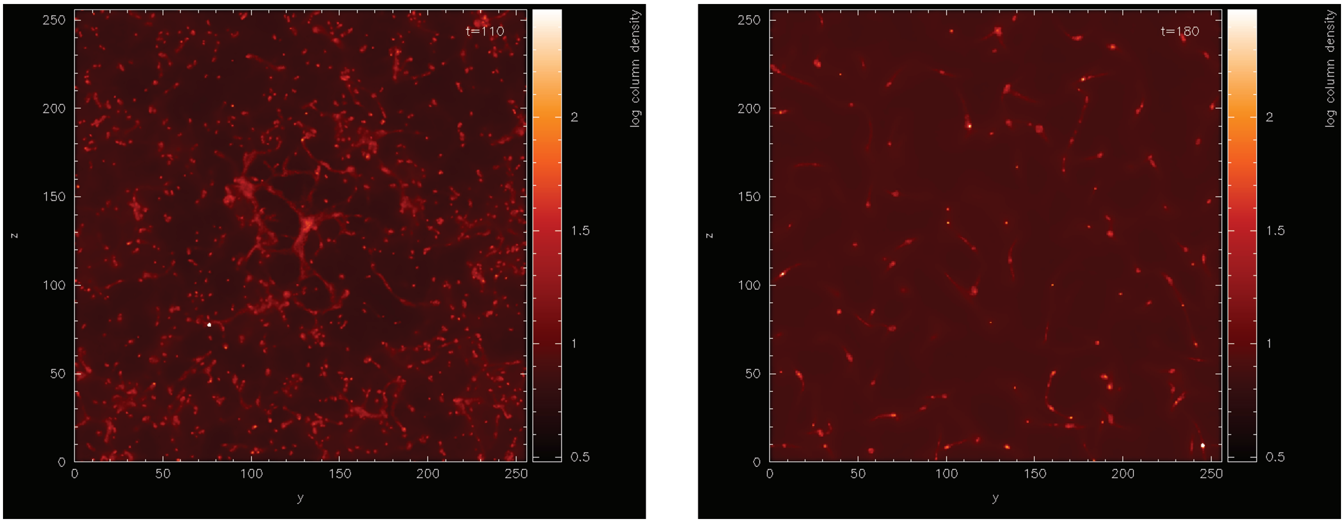

Figure 6. Face-on images (in projection) of Mi1-Mb.27-Ma2e4 (left-hand panel) and Mi0-Mb.10-Ma2e4 (right-hand panel) at the time each one is beginning to form stars. Note the scattered structure, due to the turbulence forming clumps throughout the numerical box. In run Mi1-Mb.27-Ma2e4 the colliding streams are present, but the turbulence almost completely obliterates the 'main' cloud formed by the streams (compare with the coherence of the cloud seen in Fig. 1).

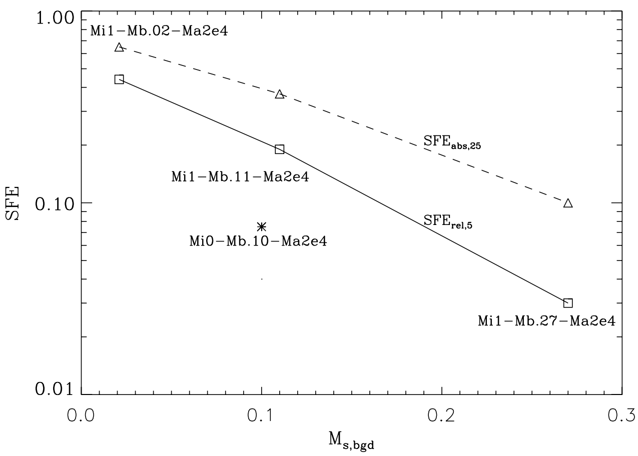

Figure 7. Dependence of $\mathrm{SFE}_{\mathrm{abs},25}$ and $\mathrm{SFE}_{\mathrm{rel},5}$ on the rms Mach number, $\mathcal{M}_{\mathrm{s,bgd}}$, of the initial (background) turbulent velocity perturbations. Both indicators are seen to decrease with increasing $\mathcal{M}_{\mathrm{s,bgd}}$ as a consequence of the progressively stronger fragmentation induced by the turbulence.

Mi1-Mb.06-Ma2e3 and Mi1-Mb.06-Ma6e2 is, respectively, $2.26 \times 10^4, 5.64 \times 10^3, 2.42 \times 10^3$ and $6.04 \times 10^2\,\mathrm{M}_{\odot}$.

Fig. 8 shows the evolution of $\mathrm{SFE}_{\mathrm{abs},25}$ and $\mathrm{SFE}_{\mathrm{rel},5}$ for these runs. We see that there is a general trend for the SFE, in both its forms, to increase with the total mass involved in the stream collision. There is only a reversal to this trend in the relative SFE between runs Mi1-Mb.02-Ma2e4 and Mi1-Mb.02-Ma5e3 because the latter has a large early maximum of $\mathrm{SFE}_{\mathrm{rel},5}$, although later it decreases, in a period of mass accumulation in the cloud at low SFR. Other than that, the trend is general, as shown in Fig. 9.

It is important to note that for all runs in this series we used the same energy injection rate of the turbulence driver. However, runs Mi1-Mb.06-Ma6e2 and Mi1-Mb.06-Ma2e3, performed in a smaller computational box, have an initial, background rms turbulent Mach number that is roughly 2.5 times larger than that of runs Mi1-Mb.02-Ma2e4 and Mi1-Mb.02-Ma5e3. This may additionally reduce the SFE because of the additional fragmentation it produces, but we see that the trend of the SFE to decrease with decreasing inflow mass holds generally even at the same physical box size, so the result appears robust.

The trend discussed above can be put in the context of the theory of KM05 for the $\mathrm{SFR}_{\mathrm{ff}}$. This theory predicts a dependence of the $\mathrm{SFR}_{\mathrm{ff}}$ on the virial parameter α and the rms Mach number $\mathcal{M}_{\mathrm{s}}$. Here,

$$\alpha \equiv 2E_{\mathrm{kin}}/|E_{\mathrm{grav}}|, \tag{5}$$

where $E_{\mathrm{kin}} = M_{\mathrm{c}}\Delta v^2/2$ is the cloud's kinetic energy, M_{c} is the cloud's mass, Δv is its rms turbulent velocity dispersion and E_{grav} is the cloud's gravitational energy.

For our flattened clouds, we compute the gravitational energy assuming they can be approximated as infinitely thin, uniform discs of radius R, and write

$$E_{\mathrm{grav}} = \int_A \Sigma\phi\, \mathrm{d}^2x = 2\pi\Sigma \int_0^R r\phi(r)\mathrm{d}r, \tag{6}$$

where A is the area of the disc, Σ is the (uniform) surface density and ϕ is the gravitational potential. In our case, the latter is given by (Wyse & Mayall 1942; Burkert & Hartmann 2004)

$$\phi(r) = -4G\Sigma R E(r/R), \tag{7}$$

where E is the second complete elliptic integral. Thus, the gravitational energy is

$$E_{\mathrm{grav}} = -8\pi G\Sigma^2 R \int_0^R rE(r/R)\mathrm{d}r = -8\pi G\Sigma^2 R^3 \int_0^1 xE(x)\mathrm{d}x$$
$$= -8\pi \left(\frac{28}{45}\right) G\Sigma^2 R^3. \tag{8}$$

To compute the kinetic energy of the clouds, we note that the relevant velocity dispersion is the one produced in the clouds as a consequence of the inflow collision (Heitsch et al. 2005; Vázquez-Semadeni et al. 2006) rather than the initial background turbulent velocity, which is much smaller. Since all four simulations analysed in this section have the same v_{inf}, we use the value of v_{rms} measured for Run Mi1-Mb.02-Ma2e4 for all of them, namely, $v_{\mathrm{rms}} = 0.5\,\mathrm{km\,s}^{-1}$. Noting that this value is a one-dimensional velocity dispersion, we take $\Delta v = \sqrt{3}\, v_{\mathrm{rms}}$.

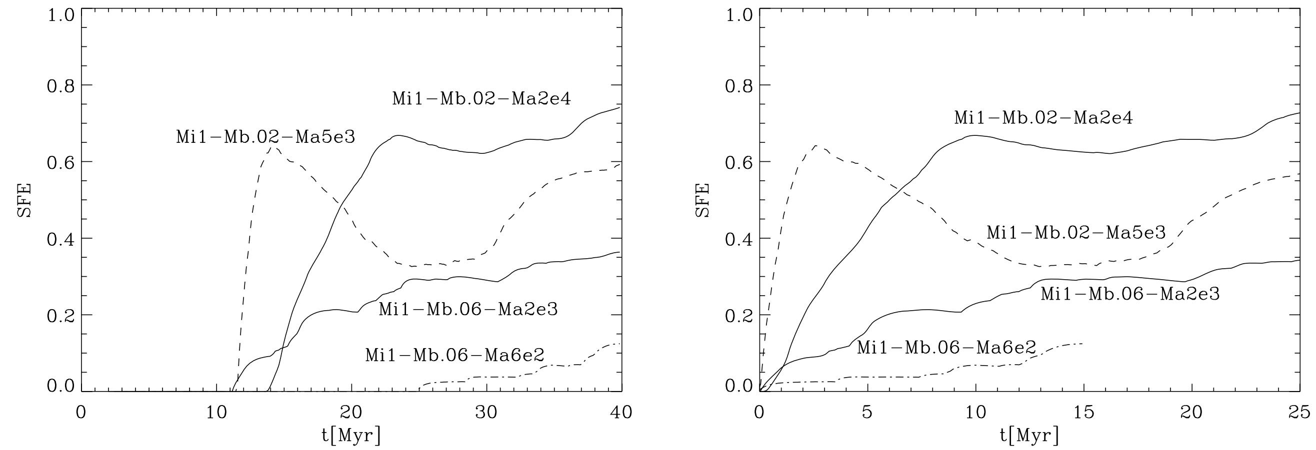

Figure 8. Evolution of the 'absolute' SFE ($SFE_{abs,25}$, left-hand panel) and the 'relative' SFE (right-hand panel) for runs Mi1-Mb.02-Ma2e4, Mi1-Mb.02-Ma5e3, Mi1-Mb.06-Ma2e3 and Mi1-Mb.06-Ma6e2. The radius of the cylindrical inflows for these runs is respectively 32, 16, 16 and 8 pc. Runs Mi1-Mb.02-Ma2e4 and Mi1-Mb.02-Ma5e3 are performed in a 256 pc box, with inflow length 112 pc, while runs Mi1-Mb.06-Ma6e2 and Mi1-Mb.06-Ma2e3 are performed in a 128 pc box with the same number of SPH particles (thus being better resolved) and a 48 pc inflow length.

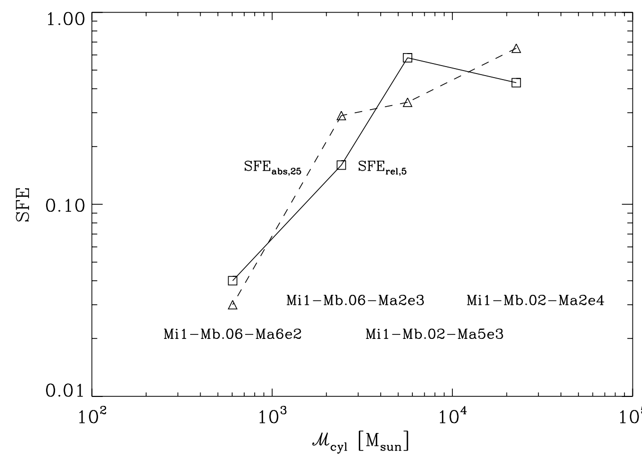

Figure 9. Dependence of $SFE_{abs,25}$ and $SFE_{rel,5}$ on the inflows' mass. A general trend for the SFE to increase with inflow mass is observed.

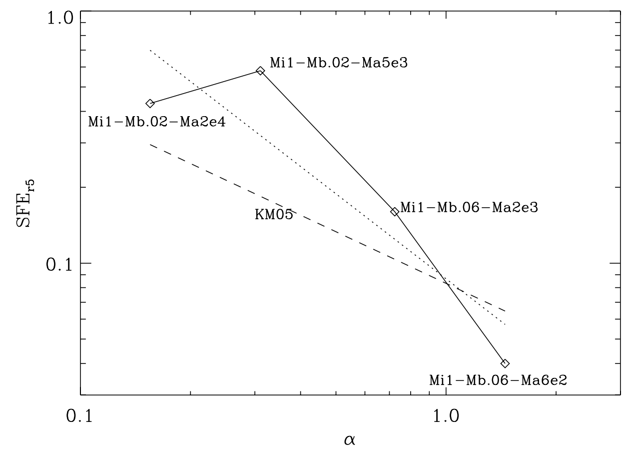

Figure 10. Dependence of $SFE_{rel,5}$ on the virial parameter α. The straight dotted line shows a least-squares fit to the simulation data, with slope -1.12, while the dashed line shows the result from KM05, with slope -0.68.

We finally obtain, from equations (5) and (8),

$$\alpha = \frac{224\pi R \Delta v^2}{45 G M_c}. \qquad (9)$$

Fig. 10 shows the results of this exercise. The solid line shows the simulation data, while the straight dotted line shows a least-squares fit to them. The dashed line shows the result from KM05, given by

$$\mathrm{SFR_{ff}} \approx 0.014 \left(\frac{\alpha}{1.3}\right)^{-0.68} \left(\frac{\mathcal{M}_s}{100}\right)^{-0.32}, \qquad (10)$$

where we have taken $\mathcal{M}_s = \Delta v / c_s$. We see that the prediction by KM05, although being numerically within the same range as the data, exhibits a significantly shallower slope. Specifically, the fit to our data has a slope -1.12 ± 0.37, where the uncertainty is the 1σ error of the fit, while the slope of the KM05 prediction, -0.68, lies beyond this error. We discuss this result further in Section 4.

4 SUMMARY AND DISCUSSION

In this paper, we have considered the scenario of MC formation by WNM stream collisions and investigated the dependence of the SFE on three parameters of this scenario, namely, the inflow speed, the rms Mach number of the background medium and the total mass contained in the inflows. Since the SFE, defined as in equation (1), is a time-dependent function because the cloud continues to accrete mass from the WNM while it forms stars, we have considered two estimators of its time integral, namely, the absolute SFE after 25 Myr from the start of the simulation, $SFE_{abs,25}$, and the 'relative' SFE, 5 Myr after the onset of SF in the cloud, denoted $SFE_{rel,5}$.

Our simulations suggest that the dominant parameter controlling the SFE is the total mass contained in the inflows, and which is eventually deposited in the forming clouds. The SFE in general decreases as the mass in the inflows is decreased. This may be a consequence of the fact that clouds formed by the collision of our inflows have all roughly the same density, temperature and velocity dispersion, so smaller clouds are more weakly gravitationally bound, a condition known to decrease the SFE (Clark et al. 2005; KM05). It is important to stress that this result is not at odds with the well-known fact that the SFE increases as the object mass decreases from the mass scale of a giant MC ($M_c \sim 10^4$–$10^6\ M_\odot$, SFE $\sim$0.02; Myers et al. 1986) to that of a cluster-forming core ($M_c \sim 10^3\ M_\odot$, SFE ∼0.3–0.5; Lada & Lada 2003), because in this case the cores' mean densities are much larger than those of the GMCs, while in our case the mean densities of the various clouds are always comparable. Thus, our clouds do not conform to Larson's (1981) density–size scaling.

The latter results, expressed in terms of the initial virial parameter of the clouds α, allow a comparison with the prediction by KM05 for the dependence of the SFE after a free-fall time (which KM05 called the $\mathrm{SFR_{ff}}$ and which is directly comparable to our $\mathrm{SFE_{rel,5}}$) with α. Although their prediction, without any rescaling, lies in the same range of values as our observed efficiencies, it involves a significantly shallower dependence on α than we observe. This may be due to the fact that those authors assumed that the clouds were supported by turbulent pressure, possibly provided by stellar feedback, while the clouds in our simulations are in general contracting gravitationally. This does not imply any shortcoming of the simulations, however, as the notion of turbulent support has been questioned recently by various works, which have suggested that the non-thermal motions implied by cloud linewidths may correspond to gravitational contraction instead (Hartmann et al. 2001; Burkert & Hartmann 2004; Hartmann & Burkert 2007; Vázquez-Semadeni et al. 2008). In particular, in our simulations, gravitational contraction of the clouds begins before the onset of sink formation, so that SF occurs in an already-contracting environment. Moreover, a recent study by Vázquez-Semadeni et al. (2010) including stellar feedback suggests that large-scale gravitational contraction is not hindered by the stellar feedback. Thus, we consider that the contracting state of our clouds is a realistic feature, and not an artefact of the absence of stellar feedback.

We have also found that the SFE decreases, although moderately, with increasing inflow velocity, measured by its Mach number, $\mathcal{M}_{\mathrm{s,inf}}$. However, we have observed that the SFRs of the runs increase with $\mathcal{M}_{\mathrm{s,inf}}$, and so the decrease in the SFE is explained because the cloud's mass accretion rate increases faster with $\mathcal{M}_{\mathrm{s,inf}}$ than the SFR. So, this whole behaviour is a consequence of the fact that the cloud is accreting from the WNM, rather than being an isolated, fixed-mass entity, and that larger inflow speeds probably cause more fragmentation in the cloud that forms, inhibiting large-scale, coherent collapse, which leads to larger SFEs, as concluded above.

Finally, we have found that the SFE also decreases with increasing background turbulence strength, as the latter progressively takes a dominant role in the production of the dense gas but, due to the relatively small scales at which the turbulence is excited compared to the scale of the inflows, the clouds and clumps formed by it are significantly smaller than the cloud formed by the coherent stream collision. Again, the smaller fragments have lower SFEs individually. This result is in sharp contrast with results from numerical simulations of decaying turbulence in which the cloud occupies the entire numerical box (e.g. Nakamura & Li 2005). This may be due to the fact that such simulations neglect the large-scale compression that forms the cloud and feeds its internal turbulence simultaneously.

ACKNOWLEDGMENTS

We thank the referee, Paul Clark, for comments and suggestions that helped us in improving this paper. The numerical simulations were performed in the cluster at CRyA-UNAM acquired with CONACYT grants 36571-E and 47366-F to EVS. GCG acknowledges financial support from grants IN106809 (UNAM-PAPIIT) and J50402-F (CONACYT). AKJ acknowledges support by the Human Resources and Mobility Programme of the European Community under the contract MEIF-CT-2006-039569.

REFERENCES

Ballesteros-Paredes J., Gazol A., Kim J., Klessen R. S., Jappsen A.-K., Tejero E., 2006, ApJ, 637, 384
Ballesteros-Paredes J., Klessen R. S., Mac Low M.-M., Vazquez-Semadeni E., 2007, in Reipurth B., Jewitt D., Keil K., eds, Protostars and Planets V. Univ. of Arizona Press, Tucson, p. 63
Bate M. R., Burkert A., 1997, MNRAS, 288, 1060
Burkert A., Hartmann L., 2004, ApJ, 616, 288
Clark P. C., Bonnell I. A., Zinnecker H., Bate M. R., 2005, MNRAS, 359, 809
Field G. B., 1965, ApJ, 142, 531
Field G. B., Blackman E. G., Keto E. R., 2008, MNRAS, 385, 181
Franco J., Shore S. N., Tenorio-Tagle G., 1994, ApJ, 436, 795
Galván-Madrid R., Keto E., Zhang Q., Kurtz S., Rodríguez L. F., Ho P. T. P., 2009, ApJ, 706, 1036
Hartmann L., Burkert A., 2007, ApJ, 654, 988
Hartmann L., Ballesteros-Paredes J., Bergin E. A., 2001, ApJ, 562, 852
Heitsch F., Burkert A., Hartmann L., Slyz A. D., Devriendt J. E. G., 2005, ApJ, 633, L113
Heitsch F., Slyz A., Devriendt J., Hartmann L., Burkert A., 2006, ApJ, 648, 1052
Hennebelle P., Pérault M., 1999, A&A, 351, 309
Hennebelle P., Mac Low M.-M., Vázquez Semadeni 2007, in Chabrier G., ed., Structure Formation in the Universe: Galaxies, Stars, Planets. Cambridge Univ. Press, Cambridge, p. 205
Jappsen A.-K., Klessen R. S., Larson R. B., Li Y., Mac Low M.-M., 2005, A&A, 435, 611
Klessen R. S., Heitsch F., MacLow M. M., 2000, ApJ, 535, 887
Koyama H., Inutsuka S.-I., 2000, ApJ, 532, 980
Koyama H., Inutsuka S.-I., 2002, ApJ, 564, L97
Kritsuk A. G., Norman M. L., 2002, ApJ, 569, L127
Kroupa P., 2001, MNRAS, 322, 231
Krumholz M. R., McKee C. F., 2005, ApJ, 630, 250 (KM05)
Lada C. J., Lada E. A., 2003, ARA&A, 41, 57
Larson R. B., 1981, MNRAS, 194, 809
Mac Low M.-M., Klessen R. S., 2004, Rev. Mod. Phys., 76, 125
McKee C. F., Ostriker E. C., 2007, ARA&A, 45, 565
Mouschovias T. C., 1991, in Lada C. J., Kylafis N. D., eds, NATO ASIC Proc. Vol. 342, The Physics of Star Formation and Early Stellar Evolution. Kluwer, Dordrecht, p. 449
Myers P. C., Dame T. M., Thaddeus P., Cohen R. S., Silverberg R. F., Dwek E., Hauser M. G., 1986, ApJ, 301, 398
Nakamura F., Li Z.-Y., 2005, ApJ, 631, 411
Padoan P., Nordlund Å., 2002, ApJ, 576, 870
Padoan P., Nordlund Å., Kritsuk A. G., Norman M. L., Li P. S., 2007, ApJ, 661, 972
Shu F. H., Adams F. C., Lizano S., 1987, ARA&A, 25, 23
Springel V., 2005, MNRAS, 364, 1105
Vázquez-Semadeni E., 2007, in Elmegreen B. G., Palous J., eds, Triggered Star Formation in a Turbulent ISM. Cambridge Univ. Press, Cambridge, p. 292
Vazquez-Semadeni E., Ostriker E. C., Passot T., Gammie C. F., Stone J. M., 2000, in Mannings V., Boss A. P., Russell S. S., eds, Protostars and Planets IV. Univ. of Arizona Press, Tucson, p. 3
Vázquez-Semadeni E., Ballesteros-Paredes J., Klessen R., 2003, ApJ, 585, L131
Vázquez-Semadeni E., Kim J., Ballesteros-Paredes J., 2005, ApJ, 630, L49
Vázquez-Semadeni E., Ryu D., Passot T., González R. F., Gazol A., 2006, ApJ, 643, 245
Vázquez-Semadeni E., Gómez G. C., Jappsen A. K., Ballesteros-Paredes J., González R. F., Klessen R. S., 2007, ApJ, 657, 870 (Paper I)

Vázquez-Semadeni E., González R. F., Ballesteros-Paredes J., Gazol A., Kim J., 2008, MNRAS, 390, 769
Vázquez-Semadeni E., Gómez G. C., Jappsen A.-K., Ballesteros-Paredes J., Klessen R. S., 2009, ApJ, 707, 1023
Vázquez-Semadeni E., Colín P., Gómez G. C., 2010, ApJ, in press
Vishniac E. T., 1994, ApJ, 428, 186
Walder R., Folini D., 2000, Ap&SS, 274, 343
Wyse A. B., Mayall N. U., 1942, ApJ, 95, 24

This paper has been typeset from a TEX/LATEX file prepared by the author.